RSC Advances

ROYAL SOCIETY OF CHEMISTRY

PAPER

View Article Online
View Journal | View Issue

Cite this: *RSC Adv.*, 2025, **15**, 48969

Enhanced mechanism of a TiO_2/g-C_3N_4 photoanode in photoelectrocatalytic synergistic persulfate activation for antibiotic degradation

Xue Zhang,[ab] Xiangpeng Gao,[c] Baowei Zhao *[a] and Nan Wu *[a]

Photocatalysis and persulfate-based advanced oxidation technologies have received considerable attention. In this study, a Z-scheme heterojunction photoanode composed of graphitic carbon nitride and titanium dioxide (TiO_2/g-C_3N_4) was constructed to develop an efficient photoelectrochemical–persulfate (PEC/PMS) activation system for antibiotic degradation. The PEC/PMS system significantly accelerated electron transfer and enhanced the photoresponse current, achieving 96.04% tetracycline removal within 12 min. The optimal operating conditions were a bias voltage of 1.0 V, a PMS concentration of 0.2 mmol L^{-1}, and a neutral to slightly alkaline environment. The system effectively resisted interference from water matrix components and achieved over 88% removal of multiple antibiotics in aquaculture pond water. TiO_2/g-C_3N_4 exhibited a Z-scheme heterostructure, and its photocatalytic activity served as the primary driving force in the synergistic process, in which degradation was dominated by radical pathways ($^{\bullet}OH$ and $^{\bullet}SO_4^-$) accompanied by a non-radical $^1O_2$ pathway. The calculated synergy factor further confirmed that the introduction of an external electric field and PMS markedly enhanced electron transfer and produced a pronounced synergistic effect.

Received 21st October 2025
Accepted 3rd December 2025

DOI: 10.1039/d5ra08080k

rsc.li/rsc-advances

1 Introduction

Photocatalytic technology (PC) is a green advanced oxidation method. However, the high recombination rate of photogenerated electron–hole pairs (e^-/h^+) limits its efficiency. Combining PC with electrocatalysis (EC) to form photoelectrocatalysis (PEC) is an effective strategy to enhance photocatalytic performance. PEC applies an external electric field to promote electron transfer and continuously directs photogenerated electrons to the cathode, thereby suppressing e^-/h^+ recombination. Electrochemical methods offer strong controllability, high stability, and no secondary pollution, and the conversion of photocatalysts into electrodes eliminates the recovery issues inherent in heterogeneous catalysts. Consequently, PEC has emerged as a promising wastewater treatment technology.[1–5]

The photoelectrochemical activity of photoanode materials plays a crucial role in the performance of PEC systems. Graphitic carbon nitride (g-C_3N_4) exhibits visible-light activity, and its band structure is appropriate for redox reactions, rendering it a highly promising semiconductor for PEC applications.[6–8] Liang *et al.* first fabricated a g-C_3N_4 photoanode for phenol degradation, where the electrocatalysis and photocatalysis exerted a synergistic promotional effect. The applied bias decreased e^-/h^+ recombination, while photocatalysis mitigated the electrode passivation caused by phenolic polymer films, thereby facilitating electrocatalytic oxidation.[9] Numerous studies have focused on enhancing the PEC performance of g-C_3N_4 using approaches such as nanoporous structure design, heteroatom doping, and heterojunction construction. Among these, coupling g-C_3N_4 with other semiconductor materials has been proven particularly effective.[10–12] TiO_2 is widely used because of its low cost, chemical stability, high catalytic activity, and corrosion resistance, and it can be integrated with g-C_3N_4 to prepare electrodes for photoelectrocatalytic applications. Huang fabricated a core–shell heterostructured photoanode by anchoring g-C_3N_4 onto TiO_2, which exhibited the excellent visible-light responsivity and significantly enhanced photoelectrocatalytic degradation efficiency. This synergistic effect accelerates the separation and migration of photogenerated carriers and the production of reactive species, resulting in a 2.4-fold improvement compared with pristine materials.[13,14] Although studies have demonstrated the excellent photocatalytic performance of g-C_3N_4/TiO_2 composites, the underlying mechanism governing the enhanced photoelectrocatalytic behaviour of g-C_3N_4 coupled with TiO_2 requires further investigation.[15,16]

Under visible-light irradiation, the catalytic performance of PEC systems depends not only on the intrinsic activity of the

[a]School of Environment and Municipal Engineering, Lanzhou Jiaotong University, Lanzhou 730070, China. E-mail: zhbw2001@sina.com; wunan0516@163.com
[b]School of Petrochemical Engineering, Lanzhou Petrochemical University of Vocational Technology, Lanzhou 730060, China
[c]Organization Department of the Communist Party of China Gansu Provincial Committee, Lanzhou 730030, China

photoelectrode but also on the electrolyte composition. The presence of strong oxidants, such as persulfate or hydrogen peroxide, enables Fenton-like oxidation, as these species can act as electron scavengers that promote electron–hole separation while being activated to generate reactive radicals.[17,18] Currently, studies combining persulfate with PEC systems have primarily focused on metal-based photoanodes, such as Bi- or W-based materials, whereas research employing g-C_3N_4 as the photoanode remains limited.[19]

In this study, a composite g-C_3N_4-TiO_2 photoanode with a direct Z-scheme heterojunction structure was fabricated and combined with peroxymonosulfate (PMS) to construct a photoelectrocatalytic–persulfate activation (PEC/PMS) system. The synergistic photoelectrocatalytic activity within the heterostructure was enhanced through improvements in photochemical performance. The effects of bias voltage, PMS concentration, pH, and water matrix components on antibiotic degradation were systematically investigated, and the degradation behaviour of multiple antibiotics in aquaculture pond water was evaluated. The enhancement mechanism of the synergistic system was elucidated through analyses of reactive oxygen species (ROS) generation pathways and reaction kinetics. The results demonstrated that photocatalysis served as the core driving force, while the combined effects of applied bias and PMS promoted electron transfer and ROS generation, enabling efficient photoanode recovery. This study provides a mechanistic basis for understanding photoelectrocatalytic persulfate activation and its potential applications.

2 Experiments and methods

2.1 Preparation of photoanode

Dicyandiamide (2 g) and ammonium oxalate (1 g) were mixed with 80 mL of deionised water, heated to 160 °C, and maintained for 8 h in a 100 mL Teflon-lined autoclave. After naturally cooling to 25 °C, the precipitate was dried at 80 °C for 8 h. The dried material was thoroughly ground and calcined at 550 °C for 4 h in a muffle furnace, followed by natural cooling and further grinding to obtain g-C_3N_4 powder. The obtained g-C_3N_4 powder and commercial nano-TiO_2 powder were mixed in methanol at a mass ratio of 1 : 1, ultrasonicated for 30 min in an 80 °C water bath, dried at 100 °C for 12 h, and finally heated at 500 °C for 10 min. After natural cooling, the product was dispersed ultrasonically in anhydrous ethanol and then coated onto ITO conductive glass to form a homogeneous slurry. The coated electrodes were dried at 50 °C, yielding a TiO_2/g-C_3N_4 photoanode for photoelectrocatalytic synergistic catalysis.

2.2 Material characterization

Scanning electron microscopy (SEM) was used to observe the micromorphology. X-ray diffraction (XRD) was employed to analyse the crystal structure. Fourier-transform infrared spectroscopy (FT-IR) was adopted to examine the surface functional groups. X-ray photoelectron spectroscopy (XPS) was used to determine the surface elemental composition and valence states as well as to measure the valence band spectra. A nitrogen adsorption analyser (BET) was adopted to determine the specific surface area, pore volume, pore size, and adsorption–desorption isotherms. UV-visible diffuse reflectance spectroscopy (UV-vis DRS) equipped with an integrating sphere was used to analyse the light absorption properties of the catalyst. Photoluminescence (PL) spectra were recorded using a fluorescence spectrophotometer. Electrochemical impedance spectroscopy (EIS), Mott–Schottky plots, transient photocurrent density measurements, linear sweep voltammetry (LSV), and light on/off photocurrent–voltage tests, as well as open-circuit potential measurements under light on/off conditions, were performed on an electrochemical workstation. The TiO_2/g-C_3N_4 electrode served as the working electrode, Ag/AgCl was the reference electrode, and a platinum plate was the counter electrode. The electrolyte was 0.5 mol per L Na_2SO_4, and the light source had a wavelength of 375 nm.

2.3 Catalytic activity test

The PEC/PMS experiments were conducted in a standard three-electrode system under the same basic conditions used for photoelectrochemical measurements. A 300 W xenon lamp equipped with a 420 nm cutoff filter served as the light source. The antibiotic concentration was 1 mg L^{-1}, and the PMS concentration was 0.2 mmol L^{-1}. Both the light source and bias potential (1.0 V) were applied simultaneously. The applied bias voltages were 0.5, 1.0, 1.5, and 2.0 V. The PMS concentrations of 0.1, 0.2, and 0.3 mmol L^{-1} and pH values of 3, 5, 7, 9, and 11 were investigated. To examine the effect of background water matrices, 10 mmol L^{-1} of humic acid (HA), Cl^-, SO_4^{2-}, CO_3^{2-}, and NO_3^- were added separately. The detailed degradation procedures are described in our previous work.[20]

2.4 Quenching experiments and capture of reactive species

Tert-butanol (TBA), methanol (MeOH), *p*-benzoquinone (BQ), β-carotene, disodium ethylenediaminetetraacetate (EDTA-2Na), and $K_2Cr_2O_7$ were employed as the quenching agents for $^{\bullet}OH$, $^{\bullet}OH$ and $^{\bullet}SO_4^-$, $^{\bullet}O_2^-$, $^1O_2$, h^+, and e^-, respectively, to identify the types of ROS involved. Electron spin resonance (ESR) spectroscopy was used for further ROS analysis. 5,5-Dimethyl-1-pyrroline-*N*-oxide (DMPO) served as a trapping agent for $^{\bullet}OH$ and $^{\bullet}O_2^-$ radicals. Notably, $^{\bullet}OH$ was trapped in the H_2O–DMPO mixture, while $^{\bullet}O_2^-$ was trapped in the MeOH–DMPO mixture. 2,2,6,6-Tetramethylpiperidine (TEMP) was adopted to trap singlet oxygen ($^1O_2$). MeOH acted as the electron scavenger, and silver nitrate ($AgNO_3$) was used as the hole (h^+) scavenger.

3 Results and discussion

3.1 Material characteristics

From the SEM images of g-C_3N_4 and TiO_2/g-C_3N_4 shown in Fig. 1(a) and (b), g-C_3N_4 was observed to consist of irregularly shaped, wrinkled, and aggregated nanosheets with a smooth two-dimensional layered structure, confirming the formation of a graphitic phase. On the surface of TiO_2/g-C_3N_4, TiO_2 nanoparticles were immobilised and aggregated on the g-C_3N_4 nanosheets, which increased the specific surface area of the

composite material.[21] The XRD pattern in Fig. 1(c) demonstrates that the characteristic diffraction peak of g-C_3N_4 at 27.8° corresponded to the (002) plane associated with the stacking of graphitic layers. In contrast, the peak at 12.9° corresponded to the (100) plane, representing the in-plane structural packing of aromatic segments and confirming the successful synthesis of g-C_3N_4. In TiO_2/g-C_3N_4, aside from the 27.8° peak of g-C_3N_4, all remaining diffraction peaks matched those of anatase TiO_2, demonstrating the coexistence of both precursors within the composite. Because TiO_2 possesses high crystallinity, the diffraction intensity of g-C_3N_4 is suppressed.[22] In the FT-IR spectra shown in Fig. 1(d), the absorption peak of g-C_3N_4 at 804 cm^{-1} was assigned to the bending vibration of tri-*s*-triazine units, whereas the peak at 890 cm^{-1} was attributed to the C–O stretching vibration induced by oxygen doping. The broad absorption band between 1720 and 1200 cm^{-1} corresponded to C–N heterocyclic stretching, and the broad band from 3260 to 3000 cm^{-1} was attributed to the N–H stretching vibrations of bridging or terminal amino groups. After coupling with TiO_2, interfacial bonding resulted in masking of several intrinsic absorption peaks of g-C_3N_4. However, the absorption features between 1720 and 1200 cm^{-1} indicated that the C–N heterocyclic framework of g-C_3N_4 remained intact.[23]

Fig. 2(a) illustrates the XPS full survey spectrum of g-C_3N_4, with photoelectron peaks at 285, 398, and 532 eV, corresponding to C 1s, N 1s, and O 1s, respectively. For TiO_2/g-C_3N_4, characteristic peaks appeared at 459 and 566 eV, corresponding to Ti 2p and Ti 2s. A significant decrease in the N content of the composite indicated the presence of nitrogen vacancies within the C–N framework. Meanwhile, the electron spin resonance signal in Fig. 2(f) indicated unpaired electrons in the conjugated aromatic structure, with a *g* value of 2.003, typical of N-vacancy sites.[24] In the C 1s spectrum of TiO_2/g-C_3N_4, a subpeak assigned to C–Ti bonding appeared, demonstrating the electronic interaction between g-C_3N_4 and TiO_2. No Ti–N peak was detected in the N 1s spectrum, likely due to the low nitrogen content. In the Ti 2p spectrum shown in Fig. 2(g), six

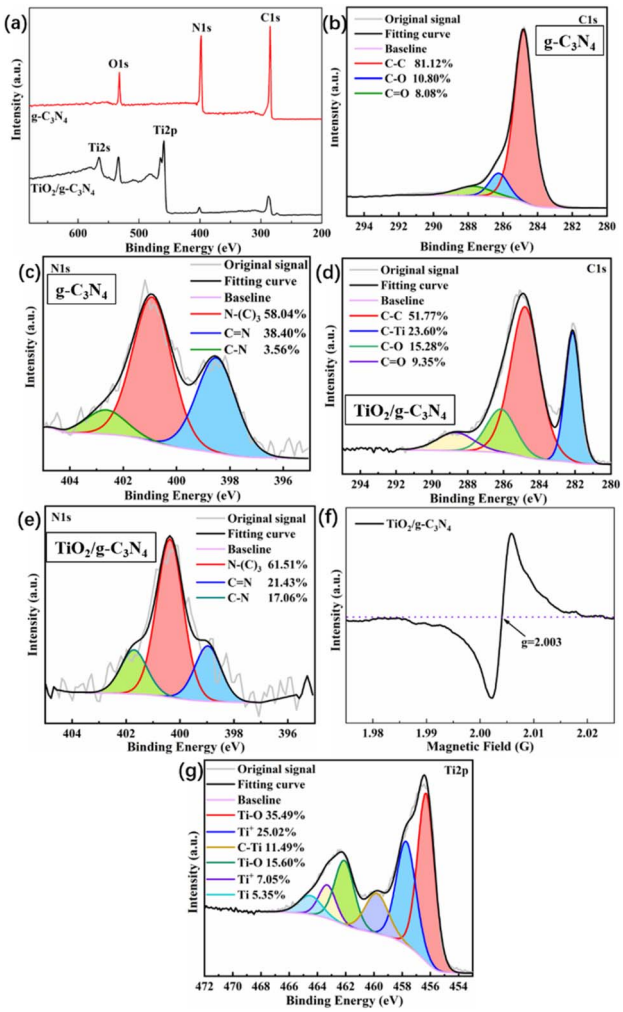

Fig. 2 XPS survey spectrum (a); high-resolution spectra of (b) C 1s and N 1s (c) for g-C_3N_4; and high-resolution spectra of C 1s (d), N 1s (e), EPR spectra (f), and Ti 2p (g) for TiO_2/g-C_3N_4.

characteristic peaks were present, among which the peaks at 457.7, 457.3 eV and 463.6, 463.3 eV correspond to Ti $2p_{3/2}$ and Ti $2p_{1/2}$, respectively. The energy difference of 5.6 eV indicates Ti^{4+} as the dominant oxidation state.[25]

Fig. 3(a) presents that both materials exhibited an H3-type hysteresis loop in their nitrogen adsorption–desorption isotherms, corresponding to a type-IV isotherm characteristic of

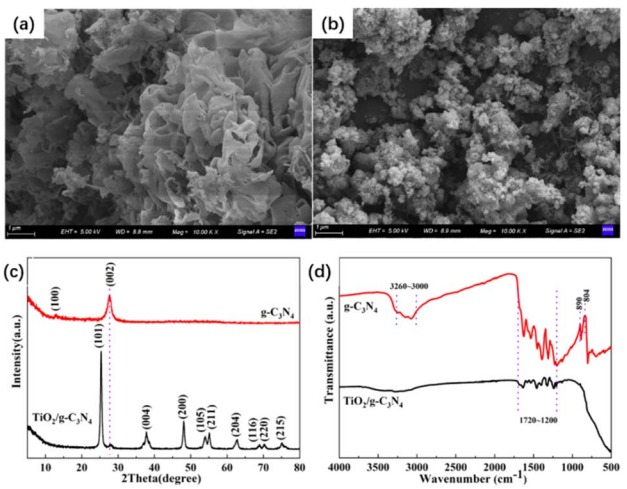

Fig. 1 SEM images of g-C_3N_4(a) and TiO_2/g-C_3N_4 (b), along with XRD patterns (c) and FT-IR spectra (d) of g-C_3N_4 and TiO_2/g-C_3N_4.

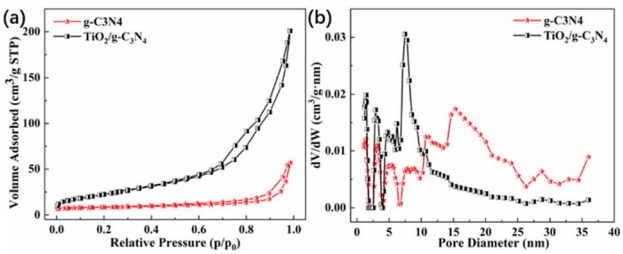

Fig. 3 N_2 adsorption–desorption isotherms (a) and pore size distributions (b) of g-C_3N_4 and TiO_2/g-C_3N_4.

lamellar cracks and micropores. The specific surface area of the composite was much larger than that of pure g-C_3N_4. As shown in Fig. 3(b), the average pore diameter of the composite was smaller than that of g-C_3N_4, consistent with the increase in the specific surface area.[26]

Fig. 4(a) shows that the UV-vis DRS spectrum of the composite material exhibited a significantly stronger absorption intensity and a considerably broader absorption range than those of the single-component materials, which contributed to the enhanced photocatalytic performance. Using the Kubelka–Munk function (Fig. 4(b)), the band gaps of g-C_3N_4, TiO_2, and TiO_2/g-C_3N_4 were calculated as 2.47, 3.05, and 2.93 eV, respectively. The electronic coupling between TiO_2 and g-C_3N_4 enhanced the absorption in both the UV and visible regions. The valence-band edges determined by VB–XPS (Fig. 4(c)) were located at 2.30 eV for g-C_3N_4, 3.01 eV for TiO_2, and 2.86 eV for TiO_2/g-C_3N_4. The band structure alignment after conversion to the NHE scale is illustrated in Fig. 4(d).[27] The Mott–Schottky plots in Fig. 4(e) present that all materials exhibited the typical n-type semiconductor behaviour, as evidenced by their positive slopes. The intercepts corresponded to flat-band potentials, further confirming the accuracy of the derived band structure. The flat-band potentials of g-C_3N_4 and TiO_2/g-C_3N_4 (*vs.* Ag/AgCl) were −0.10 and −0.03 eV, respectively, which converted to −0.32 and −0.22 eV *vs.* NHE, slightly lower than the conduction-band potentials obtained earlier.[28]

To further verify that the binary composite structure could enhance the photoelectrocatalytic performance, a series of photoelectrochemical measurements were conducted. Fig. 5(a) shows that the PL intensity of TiO_2/g-C_3N_4 was significantly lower than that of g-C_3N_4, indicating more efficient separation of photogenerated electron–hole pairs. The absence of the 460 nm emission peak in TiO_2/g-C_3N_4 may be due to the potential difference between TiO_2 and g-C_3N_4, which prevents electron transfer between the conduction bands of the coupled semiconductors and indirectly supports the presence of a Z-scheme heterojunction with superior catalytic activity.[29] Fig. 5(b) shows that the impedance arc radius of TiO_2/g-C_3N_4 was much smaller than that of g-C_3N_4, confirming the reduced interfacial electron resistance and enhanced charge transfer.[30] The LSV curves under continuous and chopped light illumination, shown in Fig. 5(c) and (d), indicate significantly improved reaction kinetics for TiO_2/g-C_3N_4, with faster electron transfer, stronger photoresponse capability, and higher concentrations of photogenerated charge carriers. Fig. 5(e) shows that TiO_2/g-C_3N_4 exhibited a higher photocurrent under visible light irradiation, which was attributed to efficient charge separation and transport. The open-circuit potential curves in Fig. 5(f) further demonstrate that the TiO_2/g-C_3N_4 heterostructure possessed markedly enhanced photocurrent responsiveness and accelerated charge transfer at the interface.[31] Together, these characterisations confirm that TiO_2/g-C_3N_4 enables faster migration and separation of photogenerated carriers and exhibits a stronger photoresponse behaviour, providing a robust foundation for its photoelectrocatalytic performance.

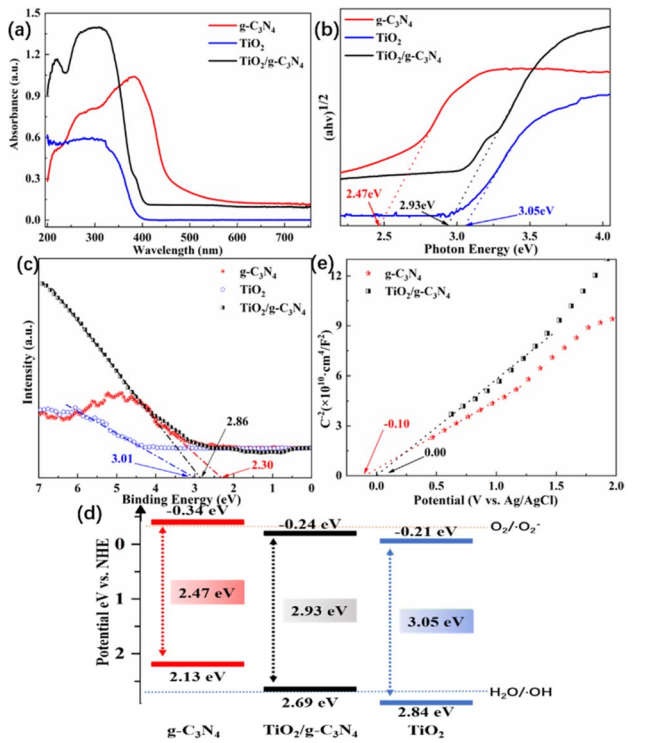

Fig. 4 UV-vis DRS spectra (a), estimated band gap (b), VB–XPS spectra (c), band gap structure alignments (d), and Mott–Schottky curves (e) of g-C_3N_4 and TiO_2/g-C_3N_4.

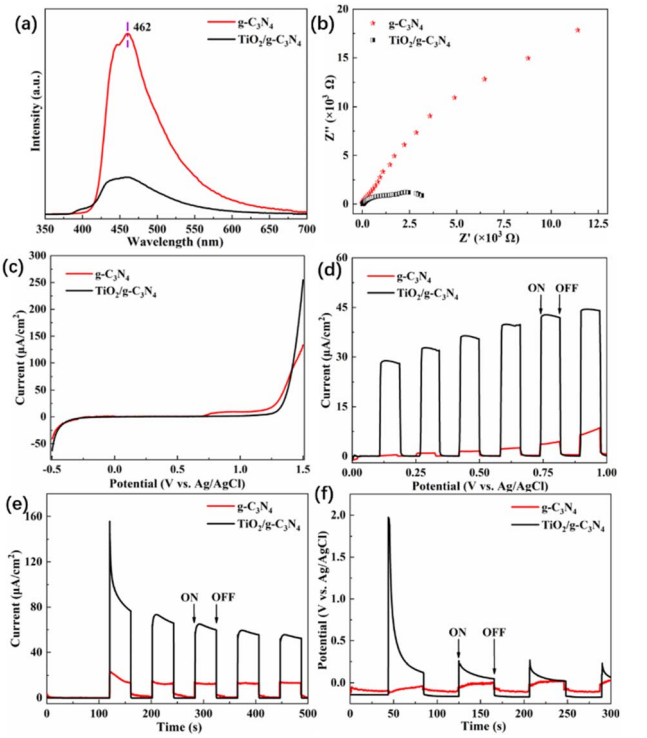

Fig. 5 PL spectra (a), EIS Nyquist plots (b), photocurrent densities *vs.* bias potential (c), current–potential curves under chopped light (d), photocurrent density plots (e), and open circuit potential under chopped light (f) for g-C_3N_4 and TiO_2/g-C_3N_4.

3.2 Analysis of photoelectrocatalytic–persulfate activation performance

To investigate the degradation performance of photoelectrocatalytic persulfate activation on tetracycline (TC) in water and to elucidate the enhancement effect of PMS on the photoelectrocatalytic system, as well as the influence of the material's photocatalytic and electrocatalytic properties on the synergistic process, a series of experiments were conducted, including PEC/PMS, electrocatalysis under visible light (PEC), photocatalysis coupled with PMS (PC/PMS), electrocatalysis coupled with PMS under dark conditions (EC/PMS), photocatalysis (PC), and electrocatalysis under dark conditions (EC). As shown in Fig. 6(a), the PEC/PMS system achieved the highest removal efficiency and the fastest degradation rate, removing 96.04% of TC within 12 min. In contrast, EC exhibited the weakest degradation performance with only 50.72% removal after 30 min. The oxidative degradation efficiencies for TC among the other systems followed the trend: PC/PMS ≈ PEC > PC > EC/PMS. Notably, the degradation efficiency under illuminated conditions was significantly higher than that in the absence of light, with removal rates exceeding 90% when irradiation was applied. These results indicate that the photocatalytic activity of the material plays a decisive role in accelerating photoelectrocatalytic reactions within the synergistic system.

The promoting effect of PMS was also evident. From an electrocatalytic perspective, the introduction of PMS increases the ionic strength of the solution and enhances mass-transfer efficiency. During the photoelectrocatalytic process, PMS undergoes electron transfer with photoexcited electrons on the surface of the photoanode, generating sulfate radicals ($^{\cdot}SO_4^-$). This increased both the diversity and concentration of ROS compared with the PEC process alone, thereby greatly enhancing the degradation capacity and overall reaction efficiency towards TC.

Kinetic analysis further clarified the differences between reaction processes. The fitting results demonstrated that the degradation reactions followed a pseudo-first-order kinetic model and that both light irradiation and PMS addition significantly increased the apparent rate constant. These findings indicate that the excellent photoelectrochemical properties of the material can provide essential conditions for the operation of the synergistic activation system and that the introduction of PMS can exert a remarkable enhancement effect. However, the PEC/PMS process is inherently complex, and its synergistic mechanism, as well as the types and generation pathways of ROS involved, will be further elucidated in the following sections.

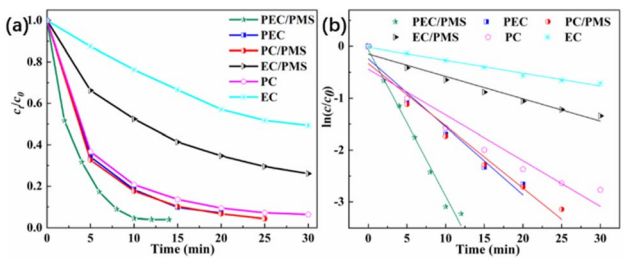

Fig. 6 TC removal efficiency using TiO_2/g-C_3N_4 under various operating conditions (a) and corresponding first-order kinetic fitting results (b). (E = 1.0 V, c_0 = 1 mg L^{-1}, c_{PMS} = 0.2 mM, pH = 7).

3.3 Analysis of influencing factors

Fig. 7(a) demonstrates that as the applied voltage increased, the current increased accordingly, requiring greater electron transfer to maintain the charge balance. This enhanced the separation efficiency of the e^-/h^+ pairs during the photocatalytic process and improved the overall degradation performance. When the voltage reached 1.5 V (*vs.* Ag/AgCl), the TC removal efficiency reached 97.33% within 10 min. The inset in Fig. 7(a) shows that k_1 increased more than twofold as the voltage increased from 0.5 to 1.5 V. At 2.0 V, the removal efficiency was lower than that at 1.0 V because excessive voltage induced side reactions on the electrode surface and hindered visible-light absorption and ROS generation. Energy consumption is a vital factor in electrochemical processes, and the specific energy consumption (E_C) was calculated using eqn (1).[32]

$$E_C = UIt \Big/ V \log \frac{c_0}{c_t} \quad (1)$$

where E_C represents the unit energy consumption (kWh m^3), U is the voltage (V), I is the average current (A), t is the reaction equilibrium time (h), V is the volume of the solution (m^3), and c_0 and c_t are the pollutant concentrations at the beginning and at equilibrium of the reaction (mg L^{-1}), respectively. The calculated E_C at 1.0 V was 0.35 kWh m^3, whereas at 1.5 V it increased to 0.58 kWh m^3. With comparable removal efficiency, the higher voltage consumed 65.71% more energy. Therefore, 1.0 V was identified as the optimal operating condition for balancing degradation efficiency and energy consumption.

Fig. 7(b) shows that increasing PMS concentration gradually enhanced the TC degradation. The promoting effect of PMS was

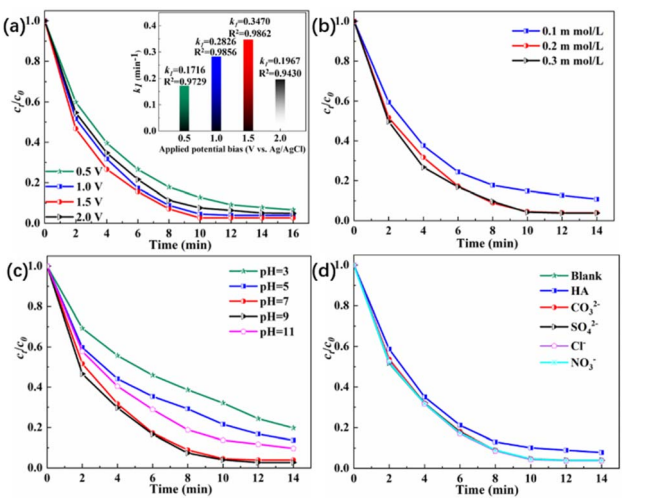

Fig. 7 (a) TC removal efficiency under various parameters. (a) Applied potential bias (c_0 = 1 mg L^{-1}, c_{PMS} = 0.2 mM, pH = 7); (b) PMS concentration (E = 1.0 V, c_0 = 1 mg L^{-1}, pH = 7); (c) pH (E = 1.0 V, c_0 = 1 mg L^{-1}, c_{PMS} = 0.2 mM); (d) background matrix in water (E = 1.0 V, c_0 = 1 mg L^{-1}, c_{PMS} = 0.2 mM, pH = 7).

discussed earlier. When the PMS concentration increased to 0.3 mmol L^{-1}, the degradation efficiency did not exhibit significant improvement. This was because excessive PMS addition could hinder timely electron transfer, restrict the generation of diverse ROS, and cause self-quenching among accumulated radicals within the system.

Fig. 7(c) shows that pH exerted a significant influence on the PEC/PMS degradation of TC, which was directly related to the ionic form of TC under different pH conditions. When the pH was below 5, the degradation efficiency was markedly inhibited because the positively charged TC tended to migrate towards the cathodic region under the electric field, preventing photogenerated holes from directly participating in oxidation. As the pH increased, TC transformed into a zwitterionic form, which was rapidly degraded by various ROS near the photoanode. However, at pH 11, the degradation efficiency decreased again. Although alkaline conditions can be favourable for PMS activation, excessive accumulation of OH^- on the photoanode surface leads to competing side reactions, such as O_2 evolution or the consumption of $^{\bullet}OH$ to form less oxidative $^1O_2$, thereby weakening the overall degradation efficiency.[33]

Fig. 7(d) shows that HA slightly inhibited the TC removal. In contrast, Cl^-, SO_4^{2-}, CO_3^{2-}, and NO_3^- had almost no effect on degradation performance. As an electron-rich organic substance, HA can compete for active sites on the photoanode, consequently suppressing the generation of $^{\bullet}SO_4^-$ and $^{\bullet}OH$ radicals and increasing the total amount of organic pollutants in the system, thus reducing the TC degradation rate.[34] Some studies have reported that CO_3^{2-} can generate weakly oxidative $^{\bullet}HCO_3^-$ radicals, whereas Cl^- can generate highly oxidative species such as HClO and $^{\bullet}Cl$. However, in this study, the anions did not significantly affect TC degradation. This was because both the weakly oxidative carbonate radicals and strongly oxidative chlorine species contributed to the propagation reactions that generated more ROS, and the opposing effects, radical quenching *versus* ROS generation, offset each other, resulting in a negligible overall influence on the degradation performance.[35]

3.4 Application in aquaculture pond water

To further evaluate the practical applicability of the PEC/PMS system, pond aquaculture water was used as the testing medium, to which TC, sulfamethoxazole (SMZ), levofloxacin (LVX), penicillin (PEN), chloramphenicol (CHL), and clindamycin (CLI) were added to assess their degradation under real aquatic conditions. The results suggest that the degradation efficiencies for all antibiotics exceeded 88%, with the degradation efficiency order of CLI > CHL > PEN > TC > LVX > SMZ. The similar removal efficiencies and corresponding k_1 values indicated that the PEC/PMS system possessed strong degradation capability towards antibiotics with different molecular structures (Fig. 8). Notably, Na_2SO_4 was not added as an electrolyte during the simulated real-wastewater experiment, rendering the treatment conditions more representative of actual environmental systems. As shown in Table 2, organic substances similar to HA present in pond water acted as quenching agents. Despite this, the PEC/PMS system still achieved favourable degradation performance, demonstrating its strong practical potential for antibiotic removal in real aquatic environments.

3.5 Analysis of PEC/PMS activation pathways and reaction enhancement mechanism

Multiple reaction modes coexisted in the PEC/PMS system. From Fig. 9(a), the quenching experiment results showed that the oxidation contribution followed the order: $^{\bullet}OH$ and $^{\bullet}SO_4^-$ > $^{\bullet}OH$ > h^+ > e^- > $^1O_2$ > $^{\bullet}O_2^-$. The contribution rates of different reactive oxygen species were further clarified using kinetic parameters.

$$R = (k_{app} - k_r)/k_{app} \quad (2)$$

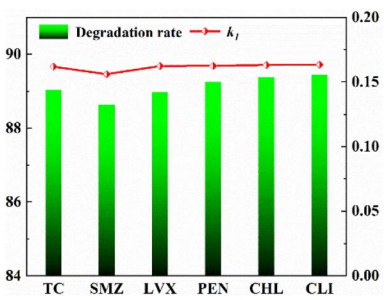

Fig. 8 Degradation performance of different antibiotics in pond water and their corresponding first-order kinetic constants. (E = 1.0 V, c_0 = 1 mg L^{-1}, c_{PMS} = 0.2 mM, pH = 7).

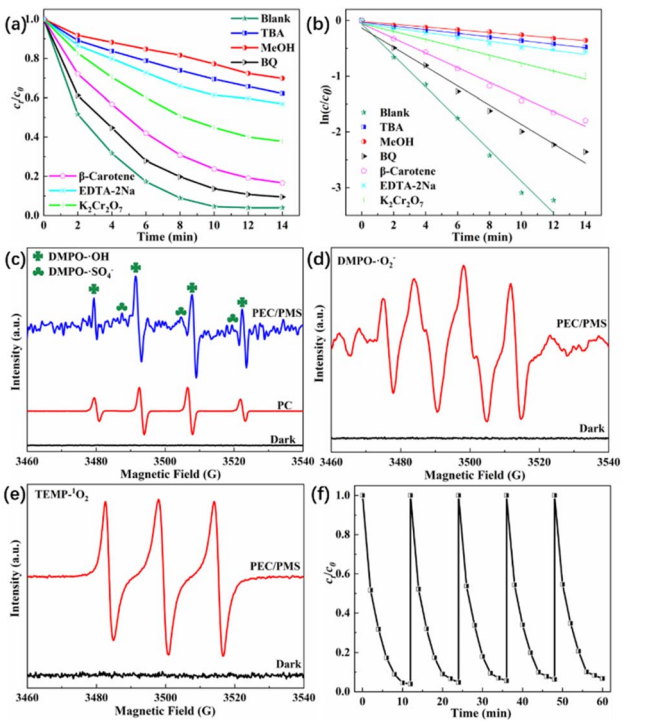

Fig. 9 Quenching experiments (a), first-order kinetic fitting results (b), and ESR spectra of $^{\bullet}OH$ and $^{\bullet}SO_4^-$ (c), $^{\bullet}O_2^-$ (d), and $^1O_2$ (e), and cyclic experiment (f). (E = 1.0 V, c_0 = 1 mg L^{-1}, c_{PMS} = 0.2 mM, pH = 7).

Table 1 First-order kinetic model parameters for different degradation modes

Degradation method	k_1 (min^{-1})	$t_{1/2}$	R^2
PEC/PMS	0.2826	2.43	0.9856
PEC	0.1314	5.27	0.9504
PC/PMS	0.1203	5.76	0.9537
EC/PMS	0.0433	16.00	0.9571
PC	0.0883	7.85	0.9082
EC	0.0247	28.06	0.9827

where R (%) represents the contribution rate of free radicals in the system. k_{app} (min^{-1}) indicates the reaction rate constant without a quencher. k_r (min^{-1}) represents the reaction rate constant after adding a quencher. The contribution rates of $^{\cdot}OH$ and $^{\cdot}SO_4^-$, $^{\cdot}OH$, h^+, e^-, $^1O_2$ and $^{\cdot}O_2^-$ were 91.26%, 88.46%, 85.88%, 74.84%, 53.40%, and 38.71%, respectively.

This indicated that the system was a composite oxidation process involving both radical and non-radical pathways, with $^{\cdot}OH$ and $^{\cdot}SO_4^-$ serving as the primary reactive species. The main ROS reaction pathways involved in this system include photocatalytic, electrochemical, and PMS-driven reactions.[36,37]

$$TiO_2/CN + h\nu \rightarrow e^- + h^+ \quad (3)$$

$$e^- + O_2 \rightarrow {}^{\cdot}O_2^- \quad (4)$$

$$h^+ + {}^{\cdot}O_2^- \rightarrow O1_2 \quad (5)$$

$$h^+ + H_2O \rightarrow {}^{\cdot}OH + H^+ \quad (6)$$

$$h^+ + OH^- \rightarrow {}^{\cdot}OH \quad (7)$$

$$^{\cdot}OH + {}^{\cdot}O_2^- \rightarrow O1_2 \quad (8)$$

$$2H_2O \rightarrow O_2 + 4H^+ + 4e^- \quad (9)$$

$$2H_2O + 2e^- \rightarrow H_2 + 2OH^- \quad (10)$$

$$h^+ + HSO_5^- \rightarrow {}^{\cdot}SO_5^- + H^+ \quad (11)$$

$$HSO_5^- + e^- \rightarrow {}^{\cdot}SO_4^- + OH^- \quad (12)$$

$$S_2O_8^{2-} + e^- \rightarrow {}^{\cdot}SO_4^- + SO_4^{2-} \quad (13)$$

$$^{\cdot}SO_4^- + H_2O \rightarrow {}^{\cdot}OH + SO_4^{2-} + H^+ \quad (14)$$

$$^{\cdot}SO_5^- + {}^{\cdot}SO_5^- \rightarrow O1_2 + 2SO_4^- \quad (15)$$

Overall, ROS generation pathways can be classified into three categories. (1) Under light irradiation, the catalyst undergoes photocatalytic reactions (eqn (3)–(8)) to generate $^{\cdot}O_2^-$, $^{\cdot}OH$, and $^1O_2$. (2) Under simultaneous light irradiation and applied bias, electrochemical reactions occur (eqn (9) and (10)) and generate O_2 and H_2. (3) After PMS addition, reactions associated with PMS generate SO_4^-, $^{\cdot}OH$, and $^1O_2$ (eqn (11)–(15)). Meanwhile, cross-linked chain reactions also occur among these ROS pathways. For example, $^{\cdot}OH$ can originate from both photocatalytic processes and persulfate activation, and both routes can further contribute to the formation of $^1O_2$, resulting in more diversified ROS species and a stronger overall oxidation capability.

Table 2 Water quality parameters of pond water

DO (mg L^{-1})	8.45	pH	7.93
COD (mg L^{-1})	12.58	DOC (mg L^{-1})	6.88
SO_4^{2-} (mM)	0.34	Cl^- (mM)	1.41
Conductivity (μS cm^{-1})	218.79	Turbidity	0.87

EPR trapping experiments also confirmed the presence of these ROS species. In addition to the characteristic $^{\cdot}OH$ signals, a comparison with the literature revealed additional $^{\cdot}SO_4^-$ peaks[38] (Fig. 9(b)). Therefore, the addition of PMS introduced $^{\cdot}SO_4^-$ radicals into the system. The presence of $^{\cdot}O_2^-$ peaks in Fig. 9(c) further verified the formation of a Z-scheme heterojunction structure. From the band structure shown in Fig. 4(d), if a type-II heterojunction was present, electrons transferred from the conduction band of g-C_3N_4 to that of TiO_2 would not possess sufficient potential to reduce O_2 to $^{\cdot}O_2^-$. Only in the Z-scheme configuration could electrons migrate from the conduction band of TiO_2 to the valence band of g-C_3N_4 and subsequently to its conduction band, where the reduction of O_2 to $^{\cdot}O_2^-$ occurred. The trapping of $^1O_2$, shown in Fig. 9(d), further confirmed the coexistence of a non-radical oxidation pathway.

Based on the kinetic data in Table 1, the synergistic activation and enhancement mechanism were analysed, and the synergistic effect of the PEC/PMS system was quantitatively evaluated using the synergy index.[39]

$$S = \frac{k_{combined} - \sum_i^n k_i}{k_{combined}} \quad (16)$$

where S represents the synergy index, $k_{combined}$ represents the reaction rate constant of the synergistic system, and k_i is the reaction rate constant of the individual system included in the

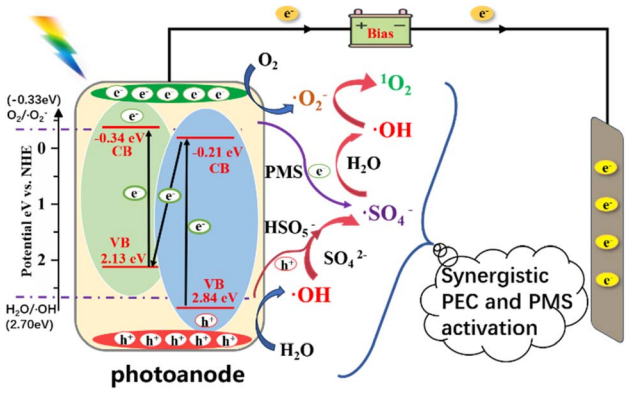

Fig. 10 Possible band structure of TiO_2/g-C_3N_4 photoanode and schematic diagram of its synergistic PEC activation mechanism for sulfate.

synergistic system. $S > 0$ denotes a synergistic effect, $S < 0$ denotes a competitive effect, and $S = 0$ denotes an cumulative effect. First, the synergy index for PEC was calculated. Compared with PC and EC, the S value was 0.14, demonstrating that the applied bias voltage promoted photocatalysis. The synergy indices of the PEC/PMS system were evaluated from two perspectives. (1) Considering PEC/PMS as the synergy of PC/PMS and EC/PMS subsystems, the S value was 0.42. (2) Considering it as a combination of PEC and PMS, the S value was 0.54. These variations clearly indicate that the synergistic effect in the PEC/PMS system increases significantly with enhanced coupling. To further evaluate system stability, five degradation cycles were conducted. As shown in Fig. 9(f), after five cycles, the system maintained high tetracycline removal efficiency, demonstrating that the photoanode exhibited strong stability.

Based on the above analysis, a reaction enhancement mechanism for the PEC/PMS system was proposed (Fig. 10). Under visible-light irradiation, photogenerated holes (h^+) and electrons (e^-) are produced within the photoanode. According to the direct Z-scheme heterojunction structure, electrons are transferred from the valence band to the conduction band of TiO_2, to the valence band of g-C_3N_4, and finally to its conduction band. This leaves strongly oxidative holes in the valence band of TiO_2, whereas electrons accumulate in the conduction band of g-C_3N_4. The photocatalytic reaction initiated under illumination serves as the primary driving force for the entire synergistic process. Under an applied bias voltage, the electron–hole pairs are rapidly separated, accelerating electron migration. The photogenerated holes directly oxidise H_2O to $^{\bullet}OH$ and activate HSO_5^- to generate $^{\bullet}SO_4^-$ radicals. Meanwhile, electrons reduce O_2 to $^{\bullet}O_2^-$. PMS, acting as an electron acceptor, also generates $^{\bullet}SO_4^-$ radicals, demonstrating that PMS addition enhances both the diversity and oxidative strength of ROS in the system. Cross-chain reactions also occur among different radicals. For example, $^{\bullet}OH$ can convert $^{\bullet}O_2^-$ into $^1O_2$, $^{\bullet}SO_4^-$ can convert H_2O into $^{\bullet}OH$, and $^{\bullet}OH$ can further activate PMS by converting SO_4^{2-} into $^{\bullet}SO_4^-$, thereby enhancing the oxidation capability of the PEC/PMS system.

4 Conclusion

In this study, g-C_3N_4 was combined with TiO_2 to enhance the synergistic effect between the heterogeneous semiconductors, thereby improving their oxidation and reduction capabilities. The photocatalytic performance was further strengthened under applied external bias voltage. Moreover, efficient and rapid degradation of antibiotics was achieved through photoelectrocatalytic synergistic activation of PMS. The TiO_2/g-C_3N_4 composite exhibited a Z-scheme heterojunction structure, which provided an efficient pathway for photogenerated charge transfer and enhanced the electron migration efficiency. The PEC/PMS system using TiO_2/g-C_3N_4 as the photoanode accelerated electron migration and increased the photoresponse current, achieving 96.04% removal of TC within 12 min. The optimal operating conditions were identified as a bias voltage of 1.0 V, a PMS concentration of 0.2 mmol L^{-1}, and a slightly alkaline environment, which effectively resisted interference from background water matrices. In aquaculture pond water, more than 88% of various antibiotics were successfully removed, demonstrating excellent practical applicability. The oxidation process was dominated by radical species (such as $^{\bullet}OH$ and $^{\bullet}SO_4^-$), with the coexistence of a non-radical $^1O_2$ pathway. The calculated synergy indices further indicated that the introduction of an electric field and PMS significantly enhanced electron transfer, exhibiting a remarkable synergistic enhancement effect.

Author contributions

Xue Zhang: conceptualization, data curation, formal analysis, writing – original draft. Xiangpeng Gao: data curation. Baowei Zhao: writing – review & editing. Nan Wu: formal analysis, resources, writing – review & editing.

Conflicts of interest

There are no conflicts to declare.

Data availability

All relevant data are within the paper.

Acknowledgements

This study was supported by Young Scholars Science Foundation of Lanzhou Jiaotong University (2022045) and the Key Research and Development Program of Gansu Province – Social Development Project under Grant No. 25YFFA014.

Notes and references

1 W. Li, G. Lv, M. Liu, F. Zhao, P. Shuai, Y. Feng, D. Chen and L. Liao, *J. Energy Chem.*, 2025, **108**, 332–360.
2 J. Sun, C. Fu, Z. Hu, I. Sirés and M. Zhou, *Crit. Rev. Environ. Sci. Technol.*, 2025, **55**(11), 783–804.
3 Y. Liu, X. Xu, X. Sun, W. Li and J. Duan, *J. Water Process Eng.*, 2025, **75**, 107911.
4 L. Ju, P. Wu, Y. Ju, M. Chen, S. Yang and H. Zhu, *Surf. Interfaces*, 2021, **23**, 100967.
5 T. Yusuf, B. Orimolade, D. Masekela, B. Mamba and N. Mabuba, *RSC Adv.*, 2022, **12**, 26176–26191.
6 A. Navidpour, D. Hao, X. Li, D. Li, Z. Huang and J. Zhou, *Catal. Rev.:Sci. Eng.*, 2024, **66**(5), 1665–1736.
7 E. Zandy, A. Bakhtiari and H. Hosseini, *Langmuir*, 2025, **41**(21), 13013–13027.
8 H. Zhuang, l. Lin, M. Xu, W. Xu and X. Li, *J. Alloys Compd.*, 2023, **969**, 172302.
9 F. Liang and Y. Zhu, *Appl. Catal., B*, 2016, **180**, 324–329.
10 J. Dong, Z. Gong, Y. Chen, G. Hao, W. Zhou, J. Li, M. Yang, R. Deng and L. Wang, *Sci. China Mater.*, 2023, **66**, 3176–3188.
11 M. Kumar, P. Haripriya and D. Kumar, *Chem. Pap.*, 2024, **78**, 8465–8472.

12 M. Saeed, A. Waseem and A. Intisar, *Catal. Surv. Asia*, 2025, **29**, 11–25.
13 M. Mansha, T. Ahmad, N. Ullah, S. A. Khan, M. Ashraf, S. Ali, B. Tan and I. Khan, *Chem. Rec.*, 2022, **22**(7), e202100336.
14 K. Huang, C. Li, X. Zhang, X. Meng, L. Wang, W. Wang and Z. Li, *Appl. Surf. Sci.*, 2020, **518**, 146219.
15 T. Bui, H. Le, H. Nguyen and V. Pham, *Mol. Catal.*, 2025, **577**, 114960.
16 Y. Luo, W. Yang, J. Liu, W. Cai, Z. Liao, X. Xiang, B. Li and Y. Fang, *Int. J. Hydrogen Energy*, 2025, **168**, 151065.
17 X. Du, X. Bai, L. Xu, L. Yang and P. Jin, *Chem. Eng. J.*, 2020, **384**, 123245.
18 J. Sun, Y. Guo, Y. Wang, D. Cao, S. Tian, K. Xiao, R. Mao and X. Zhao, *Chem. Eng. J.*, 2018, **332**, 312–320.
19 M. Petruleviciene, I. Savickaja, J. Jarosevic, J. Juodkazyte, A. Padarauskas, A. Griguceviciene and A. Ramanavicius, *ACS Omega*, 2025, **10**(8), 8538–8550.
20 N. Wu, X. Zhang, X. Zhang, K. Yang and Y. Li, *Mater. Res. Express*, 2022, **9**, 065601.
21 Q. Li, T. Zhang, D. Cuia and F. Li, *Dalton Trans.*, 2024, **53**, 7742–7750.
22 Y. Qi, H. Zhou and G. Han, *RSC Adv.*, 2025, **15**, 21300–21310.
23 A. Beizavi and M. Boroujerdni, *Ceram. Interfaces*, 2024, **50**(23), 50317–50326.
24 J. Xu and S. Ma, *J. Cryst. Growth*, 2023, **671**, 127290.
25 R. Paul, A. Das, B. Gururajan and S. Parthiban, *Diamond Relat. Mater.*, 2025, **159**, 112766.
26 L. Yang, Y. Liu, P. Tan, Y. Lu, Q. Ding and J. Pan, *Diamond Relat. Mater.*, 2023, **133**, 109727.
27 X. Chen, J. Wu, X. Wang, R. Jia, L. Li, Y. Wang, Y. Cai, Z. Chen, C. Jin, X. Wang, P. Qi, R. Wang and N. Zhang, *J. Colloid Interface Sci.*, 2025, **684**, 1049–1056.
28 W. Shi, W. Sun, Y. Liu, K. Zhang, H. Sun, X. Lin, Y. Hong and F. Guo, *J. Hazard. Mater.*, 2022, **436**, 129141.
29 F. Zhang, J. Liu, H. Yue, G. Cheng and X. Xue, *J. Mater. Sci.*, 2023, **58**, 2676–2688.
30 F. Liu, M. Fan, X. Liu and J. Chen, *Nanomaterials*, 2024, **14**(13), 1141.
31 C. Yang, X. Zhang, Y. Zhou and S. Hao, *Appl. Surf. Sci.*, 2023, **616**, 156471.
32 Z. Liu, H. Ding, C. Zhao, T. Wang, P. Wang and D. Dionysiou, *Water Res.*, 2019, **159**, 111–121.
33 Q. Yang, Y. Ma, F. Chen, F. Yao, J. Sun, S. Wang, K. Yi, L. Hou, X. Li and D. Wang, *Chem. Eng. J.*, 2019, **378**, 122149.
34 A. Son, J. Lee, C. Lee, K. Cho, J. Lee and S. Hong, *Water Res.*, 2021, **191**, 116803.
35 G. Zhang, X. Zhu, M. Yu and F. Yang, *Sep. Purif. Technol.*, 2023, **318**, 124002.
36 A. Son, J. Lee, M. Seid, E. Rahman, J. Choe, K. Cho, J. Lee and S. Hong, *Appl. Catal., B*, 2022, **315**, 121543.
37 H. Hu, H. Lin, X. Chen, Y. Pan, X. Li, Z. Zhuang, H. Chen, X. Wang, M. Luo, K. Zheng, L. Zhang and F. Chen, *Chem. Eng. J.*, 2023, **476**, 146682.
38 M. Zhang, Y. Gong, N. Ma and X. Zhao, *Chem. Eng. J.*, 2020, **399**, 125088.
39 R. Dhawle, S. Giannakopoulos, Z. Frontistis and D. Mantzavinos, *Catal. Today*, 2023, **413–415**, 114026.